Journal of Electroceramics, 15, 35–44, 2005
© 2005 Springer Science + Business Media, Inc. Manufactured in The Netherlands.

A Room Temperature Two-Step Electrochemical Process for Large Area Nanocrystalline Ferrite Thin Films Deposition

S.D. SARTALE*,† & C.D. LOKHANDE

Thin Film Physics Laboratory, Department of Physics, Shivaji University, Kolhapur, 413 003, India

Submitted June 16, 2004; Revised January 17, 2005; Accepted March 21, 2005

Abstract. In this paper, we present a room temperature two-step electrochemical process for the deposition of large area (∼10 cm^2) nanocrystalline ferrite thin films. As an example, the optimized conditions for the deposition of copper, nickel and cobalt ferrites on different conducting substrates and their physical properties are reviewed. The films are spinel in crystal structure and well adherent to the substrates. The electrical and magnetic properties of the films after annealing are comparable to the properties obtained with the films formed with other physical and chemical techniques.

Keywords: ferrite thin films, electrochemical synthesis, physical properties

1. Introduction

In recent years magnetic thin films are used in a number of devices, ranging from various versions of magnetic sensing and actuation to possible future applications in the field of spin electronics. Ferrites, the magnetic oxides having general formula MFe_2O_4 (M is divalent metal or its mixture) have extensive applications in radio, television, microwave and satellite communications, bubble devices, audio-video and digital recording and as permanent magnets [1]. Especially ferrite thin films are promising as high-density recording layers, because of their low noise characteristics and good mechanically durability [2–4]. Nowadays, there are extensive studies on ferrite thin films due to their potential applications in magnetic recording industries. Generally ferrite thin films are deposited by using physical techniques, which require high processing temperature. It is well known that deposition at high temperature is critical and affects the reproducibility and the quality of the films and suffers additionally from the environmental pollution due to the evolution of toxic gases during the deposition. In order to overcome the shortcomings arising mainly due to a high deposition process temperature, in recent years low temperature processes have been attracting increased interest for the deposition of homogeneous, fine and reproducible ferrite films [5]. In this connection we have developed a two steps electrochemical process consisting of the electrodeposition of MFe_2 (M is either divalent metal or their mixture) alloy followed by its anodization to form ferrite thin films at room temperature. Here, we present and demonstrate the viability of the idea with the large area deposition of simple systems such as $CuFe_2O_4$, $NiFe_2O_4$ and $CoFe_2O_4$ ferrite thin films [6–8]. The results reviewed here contain the study of plating variables and cathode current efficiency of electrodeposition of alloy films, anodization of alloy films to form ferrite and their characterizations.

2. Experimental

The electrochemical process used for the deposition of ferrite thin films mainly consists of two steps: electrodeposition of alloy and its anodization to form ferrite thin films at room temperature (25°C). The $CuFe_2$, $NiFe_2$and $CoFe_2$ alloy films were electrodeposited in galvanostatic mode in a two-electrode cell.

*To whom all correspondence should be addressed.
†Present address: Department of Physics, National Central University, Jungda Road 300, Jungli, Taiwan 32054. E-mail: sdsartale@phy.ncu.edu.tw; sdsartale@yahoo.com

The deposition was performed from the 100 ml bath solution on the large area ($\sim$10 cm^2) stainless steel, copper and titanium metal sheets of 1 mm thickness. All the chemicals were from commercial sources and were the highest purity (99%) available. They were used without further purification. The bath solutions were prepared using requisite amounts of metal and ferrous sulfates dissolved in double distilled water. The pH of the solution was adjusted to 2.5 by adding 0.1 M H_2SO_4. All solutions were prepared immediately prior to the deposition. A conventional three electrodes electrochemical cell was used for polarization studies. The counter electrode was graphite. Saturated calomel electrode (SCE) was used as the reference and all the potentials quoted are with respect to it.

To deposit alloy films a constant current was stabilized between the cathode and high quality graphite plate placed parallel to each other with the distance of 0.5 cm. Before deposition, the substrates were polished with smooth polish paper, degreased in alkaline solution, pickled in 0.1 M HCl to remove the rust and finally cleaned ultrasonically in distilled water. Just before the deposition, each substrate was anodically etched at a constant current density 10 mA/cm^2 for 1 min in the bath similar to that used for the deposition. The deposition was carried out at room temperature without stirring the solution. Table 1 gives the optimized conditions for $CuFe_2$, $NiFe_2$ and $CoFe_2$ alloy deposition on different substrates used in the present study.

After each deposition at a fixed charge (current $\times$ time), the film was stripped in a known volume of HCl and HNO_3 (2:1 concentrated solutions) to analyze the film composition using Perkin-Elmer atomic absorption spectrometer (AAS). Nitric and hydrochloric acids did not cause interference with the AAS measurements of copper, cobalt, nickel and iron species.

Table 1. Optimized bath composition and current density (C.D.) for the deposition of $CuFe_2$, $NiFe_2$ and $CoFe_2$ alloys on stainless steel, copper and titanium substrates. The observed film thickness and current efficiency for 30 min. deposition are also included.

Alloy	Bath composition	(C.D.) (mA/cm^2)	Thickness (μm)	Efficiency (%)
$CuFe_2$	(20 ml) 0.05 M $CuSO_4$ (80 ml) 0.1 M $FeSO_4$	9	3.8	90
$NiFe_2$	(65 ml) 0.05 M $NiSO_4$ (35 ml) 0.1 M $FeSO_4$	8	3.0	88
$CoFe_2$	(50 ml) 0.05 M $CoSO_4$ (50 ml) 0.1 M $FeSO_4$	7	3.5	94

The conversion of the alloy films deposited with the conditions given in Table 1 to the ferrites was achieved by anodizing them. Graphite was used as a cathode. The distance between alloy film and graphite plate was 0.5 cm. 1 M KOH aqueous solution was used as an electrolyte for the anodization. The anodization was carried out with the current density of 10 mA/cm^2 for 10 min. After anodization the films were washed with distilled water and preserved in the desiccator for further studies. The films were smooth, compact and covered well the substrates. After anodization, some of the ferrite thin films underwent a post-deposition annealing in air at 500°C for 1 h to improve the properties of the films.

Resulting ferrite films were investigated with respect of their different physical properties. The X-ray diffraction patterns of the films were obtained on Philips PW 3710 X-ray diffractometer using CuKα radiations operated at 25 kV and 20 mA. The infrared spectrum of the film powder was recorded by using Perkin Elmer infrared spectrophotometer model 783 in the spectral range 200–800 cm^{-1}. The pellets were prepared by mixing KBr with the film powder collected by scratching from the stainless steel substrate in the ratio 300:1 and then pressing the powder between two pieces of polished stainless steel. Morphology of the films was analyzed using scanning electron microscopy (SEM) technique. The SEM images were recorded using a LEO1530 (Gemini) FE-SEM microscope with Schottky field emission and acceleration voltage 10 kV. The films deposited on copper substrates were used to build up metal-oxide-metal (MOM) such as copper-MFe_2O_4-silver structures. The top silver electrode was either vacuum-coated or paste. The area of upper electrode was approximately 10 mm^2, so we could manage to obtain several structures on the same film. The electrical resistivity measurements were performed by means of a two probe method using same MOM structure. A constant low voltage was applied across the two electrodes and current through the film was measured as a function of temperature. The activation energy (ΔE) was calculated from the variation of DC electrical resistivity with temperature using the formula: $\rho = \rho_o \exp(\Delta E/kT)$, where ρ is electrical resistivity at temperature T, ΔE is the activation energy for electrical processes, k is Boltzman's constant and T is absolute temperature. Magnetic hysteresis loops were measured at 27°C temperature for the films deposited on copper substrates using a vibrating sample magnetometer (VSM). The magnetization field was applied parallel to the film plane. The magnetization values were derived

from the measured values divided by the volume of the films.

3. Results and Discussion

3.1. Electrodeposition of Alloy

3.1.1 Effect of Metal/Iron Ions Ratio on Alloy Film Composition. If an electrolyte contains ions of two or more metals each of which is capable of undergoing electrochemical reduction with cathode deposition, then in principle it is possible to obtain alloy of these metals of different composition. Electrodepositon of alloy can be divided into five types, regular, irregular, equilibrium, anomalous and induced [9]. Electrodeposition of binary alloys of the iron group metals (Co, Ni and Fe) exhibits the phenomenon known as anomalous codeposition [9]. In the anomalous codeposition, the less noble metal deposits preferentially; consequently, its relative content in the alloy deposit is much higher than in the solution. Another important factor, which influences the kinetics, composition and properties of electrodeposited iron group metal alloys is simultaneous hydrogen evolution. Numerous studies focusing upon the effects of additives, the presence of O_2, the inclusion of higher oxidation state of metals (M^{3+}) in the plating solution and differences in the anions have been conducted for better understanding of iron-group electrodeposition and several hypotheses have been presented in the literature [10, 11]. The effect of M^{2+}/Fe^{2+} ions ratio in the solution on the deposit composition was investigated by varying volume of the $FeSO_4$ solution in the bath. The Cu-Fe, Ni-Fe and Co-Fe alloys were electrodeposited in the bath consisting of 0.05 M metal sulfate and 0.1 M iron sulfate solutions mixed in different volume ratios. Figure 1 displays dependence of Fe content in the deposited Cu-Fe, Ni-Fe and Co-Fe alloys with the volume of 0.1 M $FeSO_4$ solution in the bath; the total volume of the bath solution was 100 ml. It is seen that the dependence of Fe content in case of Cu-Fe alloy with the Fe^{+2} ions in the bath is linear suggests that codeposition is of regular type [9]. However, in case of Ni-Fe and Co-Fe alloy depositions in lower Fe concentration range, the anomalous type of codeposition is observed. It is observed that the alloy films deposited from the bath composition at the current density given in Table 1 have the metal iron compositions as 1:2 and therefore used for further depositions.

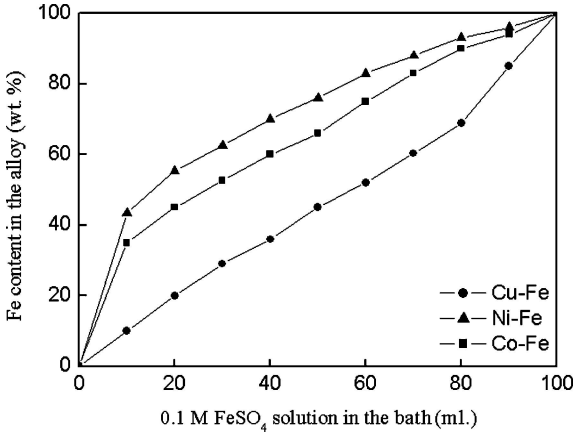

Fig. 1. Dependence of Fe content in the deposited $CuFe_2$, $NiFe_2$ and $CoFe_2$ alloys with the volume of 0.1 M $FeSO_4$ solution in the 100 ml total bath solution containing rest 0.05 M MSO_4 solution.

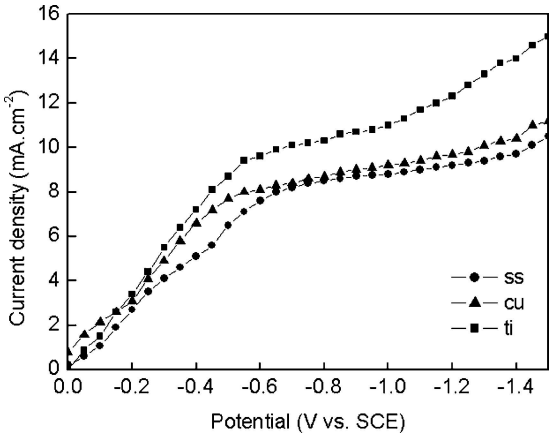

Fig. 2. Cathodic polarization curves of Cu-Fe alloy films from (20 ml) 0.05 M $CuSO_4$ and (80 ml) 0.1 M $FeSO_4$ bath solution on stainless steel (ss), copper (cu) and titanium (ti) substrates.

3.1.2 Cathodic Polarization. Figures 2–4 show the first scan polarization curves of $CuFe_2$, $NiFe_2$ and $CoFe_2$ alloys on different substrates. The deposition potentials estimated from the polarization curves (Table 2) are different for different substrates. This difference may be due to polycrystalline substrates (as evidenced by the XRD study) and different orientations of the planes from the substrate to substrate. Thus the order of mismatching between the deposited material and the substrate gives different polarization curves. Once the alloy covers the substrate, the substrate does not play a role any more. Thus for the films of

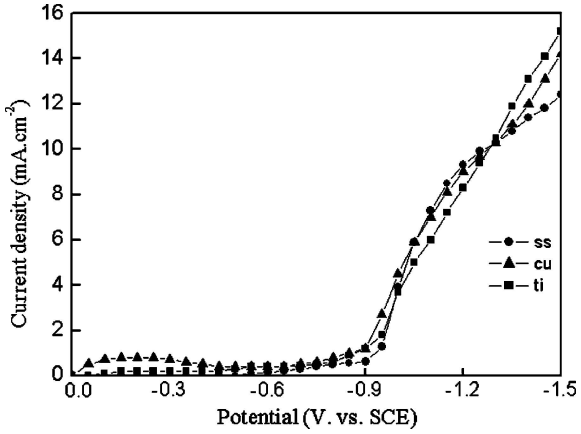

Fig. 3. Cathodic polarization curves of Ni-Fe alloy films from (65 ml) 0.05 M $NiSO_4$ and (35 ml) 0.1 M $FeSO_4$ bath solution on stainless steel (ss), copper (cu) and titanium (ti) substrates.

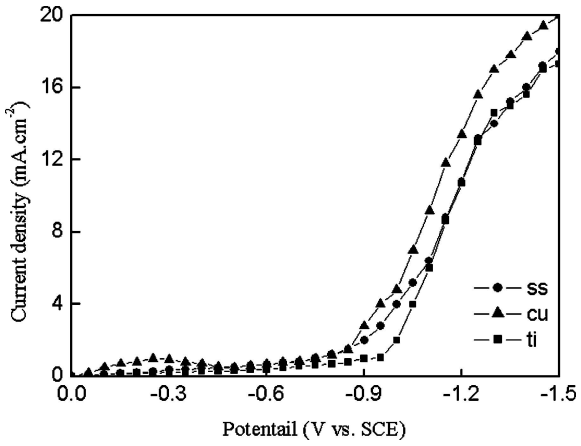

Fig. 4. Cathodic polarization curves of Co-Fe alloy films from (50 ml) 0.05 M $CoSO_4$ and (50 ml) 0.1 M $FeSO_4$ bath solution on stainless steel (ss), copper (cu) and titanium (ti) substrates.

identical roughness, identical deposition potentials are expected.

In all cases, hydrogen evolution was observed above the estimated potentials during deposition resulted into non-homogeneous film formation. It is seen that deposition potential of MFe_2 alloy is lower than the deposition potential of M and higher than the deposition potential of Fe. This might be due to the fact that deposition of noble metal takes place at lower potential when it is a constituent metal of the alloy getting deposited having another constituent metal with much less potential than the other metal [9].

Table 2. Estimated deposition potentials of MFe_2 alloys on different substrates (SS: stainless steel, Cu: copper and Ti: titanium).

	Reduction potential (V vs. SCE)		
Substrate	$CuFe_2$	$NiFe_2$	$CoFe_2$
SS	−0.89	−0.90	−0.91
Cu	−0.89	−0.96	−0.88
Ti	−0.92	−1.08	−0.97

3.1.3 Effect of Current Density on Alloy Film Thickness. From the polarization curves (Figs. 2–4) it was observed that in all cases the limiting current was about 10 mA/cm^2. Effect of current density on alloy film was studied up to 10 mA/cm^2 current density. The alloy film thickness was determined by the method of gravimetric weight difference in which area and weight of the films are measured. Before and after alloy deposition on stainless steel substrates, the films were precisely weighed; the difference of two masses gives the mass of the alloy films. The thickness was obtained by assuming the density of bulk M-Fe alloy expressed as:

$$Q = Q_M X_M + Q_{Fe} M_{Fe} \quad (1)$$

where Q_M, Q_{Fe} and X_M, X_{Fe} are the densities and the atomic fractions of M and Fe elements in the alloy. Substitution of the values of densities of M and Fe [12], and the atomic fractions determined from the AAS measurements allow us to determine the density of the alloy and thereby thickness of the alloy films.

The alloy films were deposited from the optimized bath compositions at different current densities for 30 min. Figure 5 displays the influences of current density on thickness of the $CuFe_2$, $NiFe_2$ and $CoFe_2$ alloy films deposited on stainless steel substrates. It is seen that the thickness of the alloy film decreases after the optimized current density (Table 1), possibly due to porous, foggy and less adherent film formation. Also the films may have tensile stress, which tend to cause delamination, resulting into peeling off the films from the substrates when they became thick [13]. The thickness of the films can be controlled with the deposition time in a wide range up to 5 μm at optimum current density.

3.1.4 Effect of Current Density on Efficiency of Alloy Deposition. The results of metal concentrations from AAS measurements allowed the calculations of metal and iron weight fractions for the alloy. By assuming

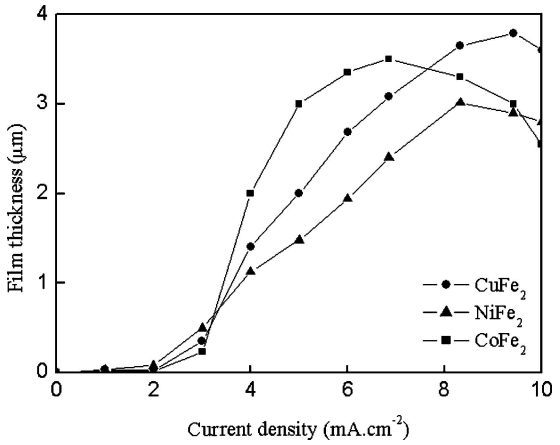

Fig. 5. Influences of the current density on thickness of the $CuFe_2$, $NiFe_2$ and $CoFe_2$ alloy films deposited on stainless steel substrates for 30 min.

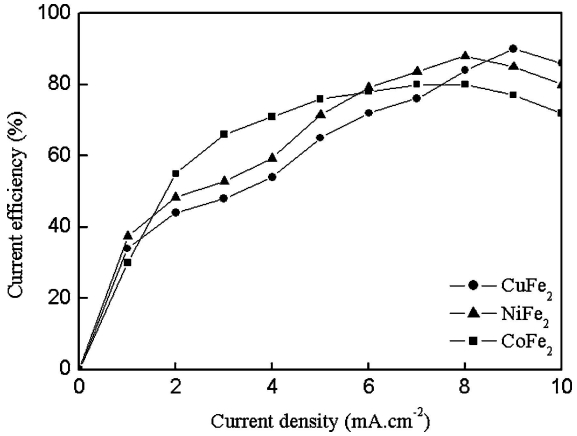

Fig. 6. The variation of cathode current efficiencies with the current density for 30 min deposition of Cu-Fe, Ni-Fe and Co-Fe alloys on stainless steel substrates.

that both single metals are reduced in two consecutive steps and considering hydrogen evolution due to the reduction of protons and dissociation of water as side reactions, current efficiency (η) of MFe_2 alloy deposition is given as

$$\eta = \frac{I_M + I_{Fe}}{I_{Total}} \tag{2}$$

where, I_M and I_{Fe} are the partial currents of the metals M and Fe calculated from the mass and composition of M and Fe in the deposit and the electrolysis charge passed using Faraday's laws. I_{Total} is the applied current, which is sum of partial currents of metals and the current utilized for side reactions. The effect of current density on current efficiency was studied to get highest efficiency.

Figure 6 shows the typical variations of cathode current efficiency with the current density for 30 min of $CuFe_2$, $NiFe_2$ and $CoFe_2$ alloy depositions on stainless steel substrates. The efficiencies increase with current density, reach maximum at optimum current density and fall for further increase in current density. Lower current efficiency below optimum current density can be attributed to the decrease in the rate of deposition of metals to a point, where hydrogen evolution is the dominant reaction on the cathode [11]. Further increase in current efficiency above optimum current density only leads to an increase in the rate of hydrogen evolution due to the reduction of water molecules [14]. This results in decrease of the current efficiency above optimum current density.

The optimized plating bath composition and current density for the deposition of $CuFe_2$, $NiFe_2$ and $CoFe_2$ alloy films on different substrates are given in Table 1 with the observed thickness and current efficiencies.

3.2. *Anodization of the Alloy to Form Ferrite*

In aqueous solution after application of potential, the reactions occurring at cathode and anode are as follows :

$$M + 2OH^- \rightarrow MO + H_2O + 2e^- \quad \text{(anode)} \tag{3}$$

$$2e^- + 2H_2O \rightarrow H_2 \uparrow + 2OH^- \quad \text{(cathode)} \tag{4}$$

The reactions indicate that oxide films are grown on the anode surface and hydrogen is evolving at cathode.

Table 3. The crystal structure and positions of IR absorption high frequency (ν_1) and low frequency (ν_2) bands observed for (A) as deposited and (B) annealed $CuFe_2O_4$, $NiFe_2O_4$ and $CoFe_2O_4$ thin films.

	$CuFe_2O_4$		$NiFe_2O_4$		$CoFe_2O_4$	
Film	A	B	A	B	A	B
Crystal structure	Tetragonal	Tetragonal	Cubic	Cubic	Cubic	Cubic
$\nu_1(cm^{-1})$	590	610	620	590	620	600
$\nu_2(cm^{-1})$	390	380	410	400	410	400

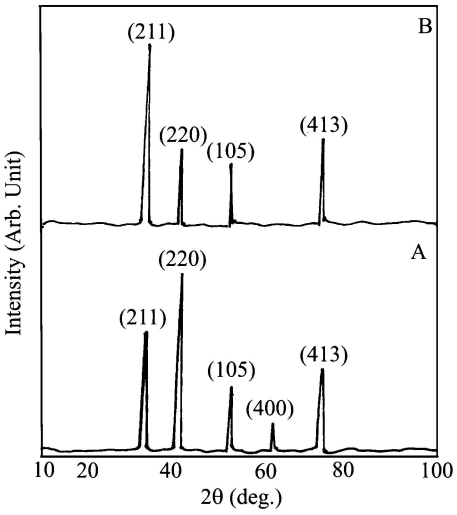

Fig. 7. Typical XRD patterns of (A) as deposited and (B) annealed $CuFe_2O_4$ films deposited on stainless steel substrates.

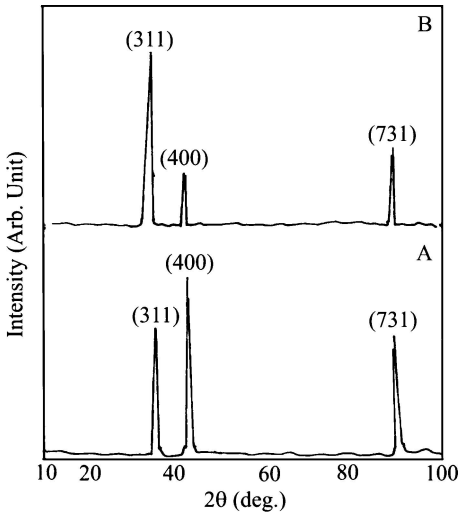

Fig. 8. Typical XRD patterns of (A) as deposited and (B) annealed $NiFe_2O_4$ films deposited on stainless steel substrates.

In the present investigation, the conversion of MFe_2 alloy to ferrite (MFe_2O_4) can be explained with the following reaction.

$$MFe_2 + 8OH^- \rightarrow MFe_2O_4 + 4H_2O + 8e^- \quad (5)$$

The MFe_2 alloy films were converted to ferrite (MFe_2O_4) thin films by using anodization at 10 mA/cm^2 current density for 10 min. It should be noted that anodization charge (current density and time) was less for the alloy films with lower thickness.

3.3. Structure and Morphology

The crystal structures of the ferrite films were investigated by using X-ray diffraction (XRD) technique. The comparison of the observed '*d*' values with the standard JCPDS [15–17] values revealed that the films are polycrystalline with spinel tetragonal $CuFe_2O_4$ and cubic $NiFe_2O_4$ and $CoFe_2O_4$ structures. Typical XRD patterns of as deposited and annealed $CuFe_2O_4$, $NiFe_2O_4$ and $CoFe_2O_4$ films deposited on stainless steel substrates are displaced in Figs. 7–9. Similar structures were observed for other substrates. It is seen from the XRD patterns that after anodization the alloy films are converted to spinel ferrite at room temperature. It is also observed that after annealing the characteristics peaks of bulk ferrites corresponding to (211) of $CuFe_2O_4$ and (311) of $NiFe_2O_4$ and $CoFe_2O_4$ became sharper and more intense. We attribute this improvement in intensity of these characteristic peaks to the crystallization of the films towards bulk materials. In order to evaluate the mean crystallite size of the films, the Scherrer's formula was adopted. The mean crystallite sizes of the films were below 50 nm suggesting that the films are nanocrystalline. The nanocrystalline nature of the films is an advantageous factor to obtain high efficient magneto-optic recording devices [18].

Table 4. The observed room temperature (27°C) electrical resistivity (ρ) and activation energy (ΔE) values of (A) as deposited and (B) annealed $CuFe_2O_4$, $NiFe_2O_4$ and $CoFe_2O_4$ films deposited on copper substrates.

	$CuFe_2O_4$		$NiFe_2O_4$		$CoFe_2O_4$	
Electrical property	A	B	A	B	A	B
$\rho(\Omega\cdot$ cm)	1.73×10^9	2.51×10^8	6.31×10^7	3.46×10^7	6.31×10^7	1.55×10^7
(ΔE) (eV)	0.49	0.48	0.30	0.29	0.45	0.46

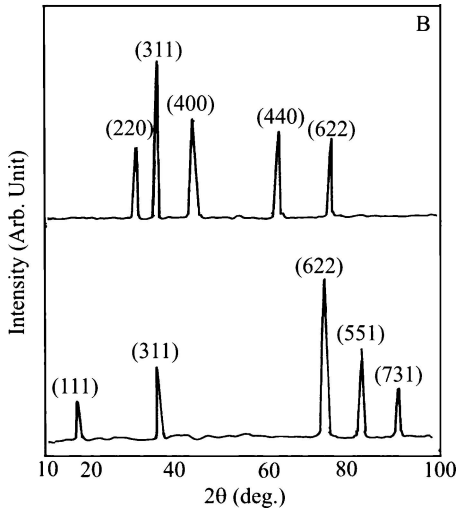

Fig. 9. Typical XRD patterns of (A) as deposited and (B) annealed $CoFe_2O_4$ films deposited on stainless steel substrates.

Further, IR absorption spectroscopy was used to verify the spinel structure of the films. It is observed that positions of the high and low frequency bands of as deposited and annealed $CuFe_2O_4$, $NiFe_2O_4$ and $CoFe_2O_4$ films were at around 600 and 400 cm^{-1}, which confirm the spinel structures of the films [19]. The observed band positions for powders of as deposited and annealed $CuFe_2O_4$, $NiFe_2O_4$ and $CoFe_2O_4$ films are given in Table 3. Different band position in the spectra for as deposited and annealed films can be attributed to different size and shape of the particles.

Typical SEM micrographs of annealed $CuFe_2O_4$, $NiFe_2O_4$ and $CoFe_2O_4$ films deposited on stainless stell substrates are displayed in Fig. 10. It is observed that copper ferrite films show better morphology than nickel and cobalt ferrite films. The rough morphology of the films with pin holes may be occurred during anodization.

3.4. Electric Properties

The temperature variations of electrical resistivity of as deposited and annealed $CuFe_2O_4$, $NiFe_2O_4$ and $CoFe_2O_4$ films deposited on copper substrates are shown in Figs. 11–13. It is clear from the figures that the resistivity increases as temperature decreases, showing a semiconducting behaviour. Observed room temperature resistivities and activation energies are given in

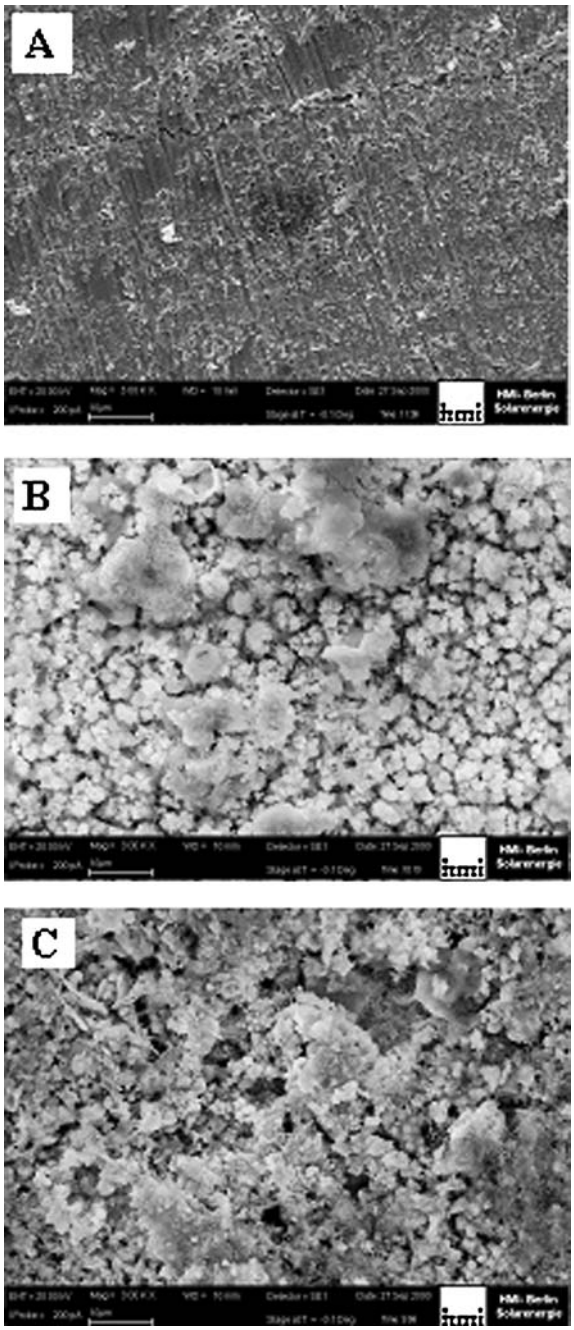

Fig. 10. Typical SEMs of annealed (A) $CuFe_2O_4$, (B) $NiFe_2O_4$ and (C) $CoFe_2O_4$ films deposited on stainless steel substrates.

Table 4. The observed resistivities are higher and calculated activation energies are comparable to the values reported for the films or bulk samples prepared by other physical or chemical techniques [20–23]. We attribute

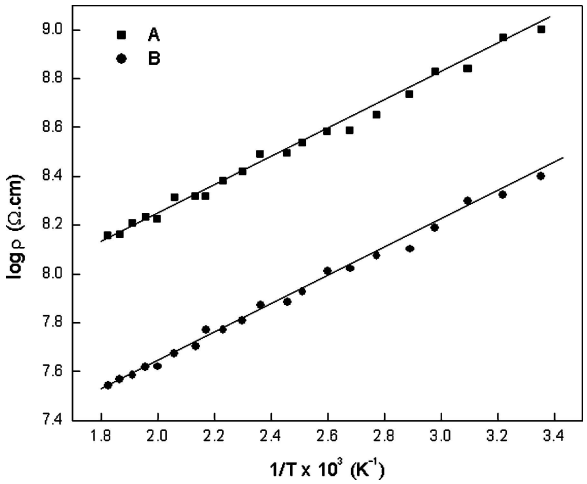

Fig. 11. Plot of log of electrical resistivity (ρ) against reciprocal of temperature for (A) as deposited and (B) annealed $CuFe_2O_4$ films deposited on copper substrates.

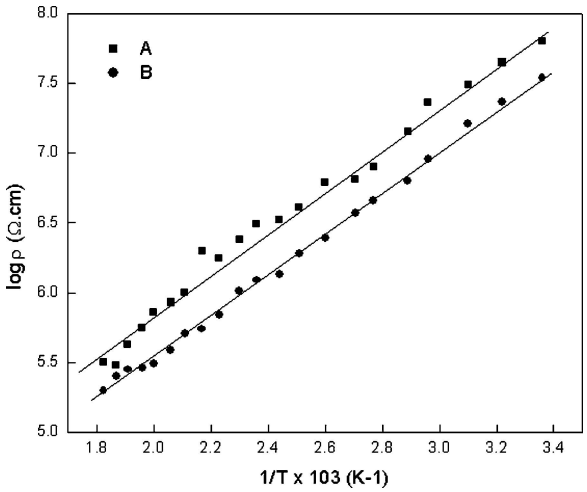

Fig. 12. Plot of log of electrical resistivity (ρ) against reciprocal of temperature for (A) as deposited and (B) annealed $NIFe_2O_4$ films deposited on copper substrates.

higher resistivity of the films to nanocrystalline nature and rough surface morphology. The change in activation energies for as deposited and annealed films is not appreciable. It is observed that after annealing resistivity decreases may be due to increase in grain size or change in crystallographic texture and decrease in defects and dislocations.

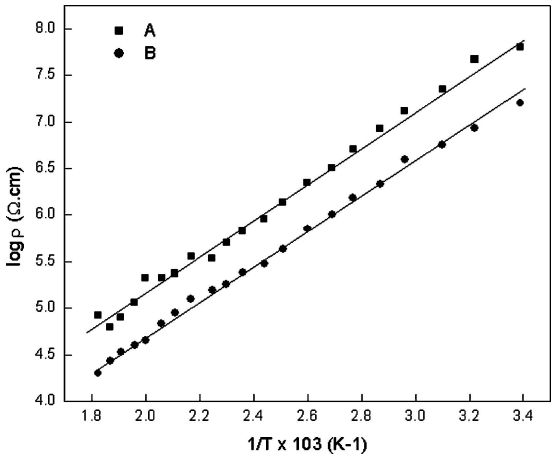

Fig. 13. Plot of log of electrical resistivity (ρ) against reciprocal of temperature for (A) as deposited and (B) annealed $CoFe_2O_4$ films deposited on copper substrates.

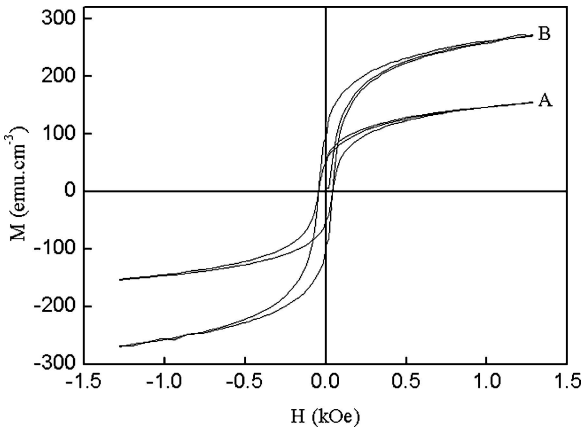

Fig. 14. Magnetic hysteresis curves measured for (A) as deposited and (B) annealed $CuFe_2O_4$ films deposited on copper substrates.

3.5. Magnetic Properties

The magnetic hysteresis curves measured for $CuFe_2O_4$, $NiFe_2O_4$ and $CoFe_2O_4$ ferrite films deposited on copper substrates are displayed in Figs. 14–16. The saturation magnetization (Ms), coercive field (Hc) and residual magnetization (Mr) values are determined from the curves. Table 5 summarizes the magnetic properties of the ferrite films (A) before and (B) after annealing. It is seen that the Ms and Hc of the as deposited films are enhanced and Mr reduced after annealing. The enhancement of Ms and Hc and reduction in Mr can be

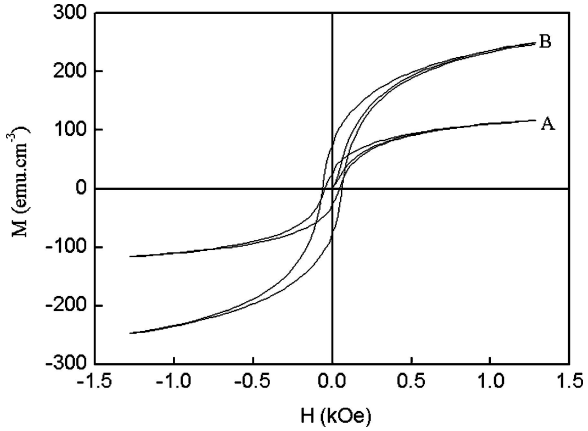

Fig. 15. Magnetic hysteresis curves measured for (A) as deposited and (B) annealed $NiFe_2O_4$ films deposited on copper substrates.

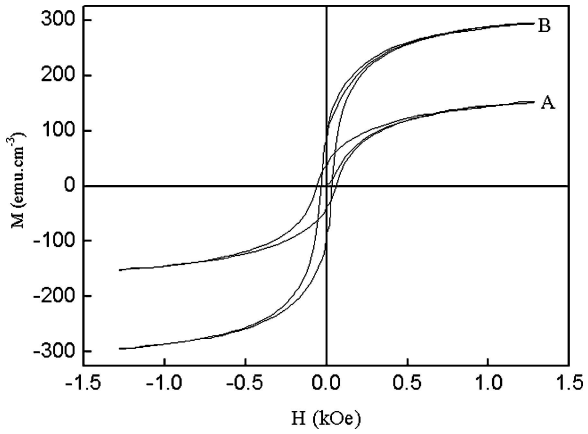

Fig. 16. Magnetic hysteresis curves measured for (A) as deposited and (B) annealed $CoFe_2O_4$ films deposited on copper substrates.

attributed to increase in particle size with improved crystallinity after annealing [22]. The magnetic properties of the films possessed after annealing are comparable to the reported values of films prepared by other techniques [24–28].

4. Conclusions

We demonstrated the novel two-step electrochemical process for the deposition of larger area nanocrystalline ferrite (MFe_2O_4, M is Cu, Ni, Co, Mg, Mn, Zn, and Cd or their mixtures) thin films at room temperature. This process consists of two steps, namely, electrodeposition of alloy followed by its anodization to convert alloy into ferrite thin film at room temperature. This method facilitates the deposition of different ferrite thin films on large area substrates with thickness up to 5 μm from aqueous medium without any high vacuum and/or temperature. Feasibility of the process is checked by depositing simple systems such as $CuFe_2O_4$, $NiFe_2O_4$ and $CoFe_2O_4$. The physical properties of the films are promising after annealing and therefore our process is a suitable alternative to other techniques used for ferrite thin films formation. Thus, it opens a new channel for the investigation of other promising simple or mixed ferrite films useful in optoelectronic and magnetic recording industries.

Table 5. The determined values from the hysteresis curves of saturation magnetization Ms (emu/cm^3), coercive field, Hc (kOe) and residual magnetization, Mr (emu/cm^3) of (A) as deposited and (B) annealed $CuFe_2O_4$, $NiFe_2O_4$ and $CoFe_2O_4$ thin films deposited on copper substrates.

	$CuFe_2O_4$		$NiFe_2O_4$		$CoFe_2O_4$	
Magnetization values	A	B	A	B	A	B
Ms	155	267	117	246	151	293
Mr	59	95	24	99	36	104
Hc	0.05	0.05	0.05	0.06	0.05	0.03

Acknowledgment

Authors are thankful to Dr. Alok Banerjee, IUC-DAEF, Indore, India for the help in VSM measurements.

References

1. B. Viswanathan and V.R.K. Murthy, *Ferrite Materials* (Springer-Verlag, Berlin 1990).
2. F. Cheng, Z. Peng, Z. Xu, C. Liao, and C. Yan, *Thin Solid Films*, **339**, 109 (1999).
3. D.M. Schleich and Y. Zhang, *Mater. Res. Bull.*, **30**, 447 (1995).
4. I. Nedkov, T. Merodiiska, L. Milenova, and T. Koutzarova, *J. Magn. Magn. Mater.*, **211**, 296 (2000).
5. M. Abe, *MRS Bull.*, **25**, 51 (2000).
6. S.D. Sartale and C.D. Lokhande, *Mater. Chem. Phys.*, **70**, 274 (2001).
7. S.D. Sartale and C.D. Lokhande, *Ind. J. Mater. Sci. Engg.*, **7**, 404 (2000).
8. S.D. Sartale and C.D. Lokhande, *Ceramic International*, **28**, 467 (2002).

9. A. Brenner, *Electrodeposition of alloys. Vol. I and II* (Academic Press, New York 1963).
10. K. Sasaki and J.B. Talbot, *J. Electrochem. Soc.*, **147** (2000) 189, and references therein.
11. N. Zech, E.J. Podlaha, and D. Landolt, *J. Electrochem. Soc.*, **146** (1999) 2886, and references therein.
12. *CRC Hand Book of Chemistry and Physics*, 79th edition, edited by D.R. Lide, (CRC Press, Boca Raton FL, 1998–1999).
13. Y. Kitamoto and M. Abe, *J. Phys. IV France*, **7**, C1-595 (1997).
14. V. Narasimhamurthy and B.S. Sheshadri, *Metal Finishing*, **95**, 44 (1997).
15. JCPDS-ICDD Card no. 34-425; 1994.
16. JCPDS-ICDD Card no. 44-1485; 1994.
17. JCPDS-ICDD Card no: 22-1086; 1994.
18. F. Cheng, Z. Peng, C. Liao, Z. Xu, S. Gao, C. Yan, D. Wang, and J. Wanh, *Solid State Commn.*, **107**, 471 (1998).
19. R.D. Waldron, *Phys. Rev.*, **99**, 1727 (1955).
20. S.A. Mazen, *Mater. Chem. Phys*., **62,** 131 (2000).
21. C. Jovalekic, M. Zdujic, A. Radakovic, and M. Mitric, *Mater. Lett.*, **24,** 365 (1995).
22. M.S. Lee, T.Y. Kim, C.S. Lee, J.C. Park, Y.I. Kim, and D. Kim, *J. Magn. Magn. Mater.*, **268**, 62 (2004).
23. S.S. Bellad and C.H. Bhosale, *Thin Solid Films*, **322**, 93 (1998).
24. M. Desai, S. Prasad, N. Venkataramani, I. Samajdar, A.K. Nigam, and R. Krishnana, *J. Appl. Phys.*, **91**, 2220 (2002).
25. I. Nedkov, T. Merodiska, L. Milenova, and T. Koutzarova, *J. Magn. Magn. Mater.*, **211**, 296 (2000).
26. T. Tsuchiya, H. Yamashiro, T. Sei, and T. Inamura, *J. Mater. Sci.*, **27,** 3645 (1992).
27. F. Cheng, Z. Peng, C. Liao, Z. Xu, S. Gao, C. Yan, D. Wang, and J. Wang, *Solid State Comm.*, **107**, 471 (1998).
28. T.H. Hai, H.T.B. Van, T.C. Phong, and M. Abe, *Physica B*, **327**, 194 (2003).